CHAPTER 4

Empirical and Process Studies

CDC conducts diverse research activities that span time scales from intraseasonal to decadal. Whereas other chapters focus on specific time bands, this chapter considers basic physical processes important in climate variability that occur across time scales. Moist atmospheric convection, clouds and climate, atmospheric angular momentum, and air-sea interaction are topics of active research. CDC scientists integrate modeling and observations to better understand physical processes, and to overcome limitations in either observational or modeling analyses alone. Coherent phenomena such as ENSO, the Madden-Julian oscillation (MJO) and the seasonal cycle provide specific case studies and important examples of scale interactions.

Moist atmospheric convection is central to all climate phenomena studied at CDC and epitomizes the complexity of the climate system. At CDC, we use observations and hierarchical modeling to conduct fundamental studies of moist convection in various environments. A key objective is to evaluate the assumptions at the heart of present day cumulus parameterization schemes. Cloud-resolving models are used to develop, test and refine parameterizations in a simplified and tractable context.

Clouds also profoundly impact climate variability. CDC research shows that stratocumulus decks over the east Pacific influence the seasonal cycle of sea surface temperature (SST). The three-dimensional structure of clouds helps determine the heating that drives such ocean-atmosphere interactions, and must be properly represented in climate models. CDC scientists have developed a simple cloud overlap scheme for GCMs, and are working on a higher order statistical cloud scheme to better represent the subgrid scale distribution of cloud properties.

A key feature of tropical variability is the MJO, which produces strong air-sea interactions over the warm pool and may influence the ENSO cycle, particularly the onset and decay phases. CDC scientists determined that SST anomalies within the MJO are driven mainly through surface energy fluxes, especially shortwave and latent heat fluxes. MJOs were also shown to play a prominent role at the onset of the 1997–98 El Niño event. MJO events initiated cooling of SSTs in the west Pacific via surface fluxes and warming in the central Pacific via Kelvin wave currents. In the first link identified with interannual SSTs, CDC scientists found that strong MJO activity during the northern winter was correlated with positive SSTA in the western Pacific during the preceding northern fall.

Most prediction models systematically lose atmospheric angular momentum (AAM) during the forecast cycle, a serious concern for such a fundamental quantity. CDC scientists used studies of the AAM budget to demonstrate the negative impact of gravity wave drag, including its role in local and global systematic forecast errors. CDC scientists also constructed a linear model of global AAM anomalies that replicated much of the observed intraseasonal variability and clarified the role of the mountain and friction torque in AAM variations. Composite studies were used to illustrate the regional patterns that produce the torques and helped identify a mid-latitude mode with a time scale similar to the MJO.

The diverse range of activities described in this chapter illustrates the breadth of CDC diagnostics research, provides insight and understanding of different physical processes, and provides a foundation for assessment of climate models.

4.1. Moist atmospheric convection

Understanding moist atmospheric convection and its influence on climate variability is central to empirical and process studies at CDC. It links small-scale turbulent motions to global circulations through cloud formation and precipita-

tion. It connects the slowly varying conditions at the Earth's surface to the faster atmospheric responses, providing much of the long-term predictability of atmospheric circulations. Furthermore, it is the proximate cause of many climate impacts on humanity (e.g., drought, flood, and severe weather) and contributes significantly to systematic errors in climate and forecast models. In light of the complexity of convective processes and the wide range of space and time scales involved, a diverse and opportunistic research strategy has been adopted. This research draws on a wide range of models and observations, from cloud-resolving to planet-spanning, from highly idealized to highly realistic.

CDC scientists have developed a new analysis technique called cylindrical binning that facilitates statistical studies using large Doppler radar data sets. Making effective use of existing data, the relationship between rainrate and horizontal wind divergence (**Fig. 4.1**), which is fundamental to the interaction of mesoscale convection and large-scale

circulations, is explored. Here, wind divergence (the line integral of Doppler velocity around a circle centered on the radar) at every level in the atmosphere is regressed onto hourly area-averaged surface rain rate (estimated from reflectivity). Color indicates the size of the circle over which averages are considered. All the profiles exhibit the expected low-level convergence and upper-level divergence. Other interesting features are present that indicate, among other things, the spatial scale of the convective systems. However, the statistical significance and physical interpretation of those features remains uncertain and is a subject of further study.

A more detailed and quantitative, if synthetic, source of data about convection is cloud-resolving models. With increasing computer power, ambitious computations are being performed around the world, and some of the resulting data sets are being analyzed at CDC. For example, **Fig.4.2** shows a vertical velocity field at 1500m altitude in a 1064x32 doubly-periodic cloud-resolving model Convec-
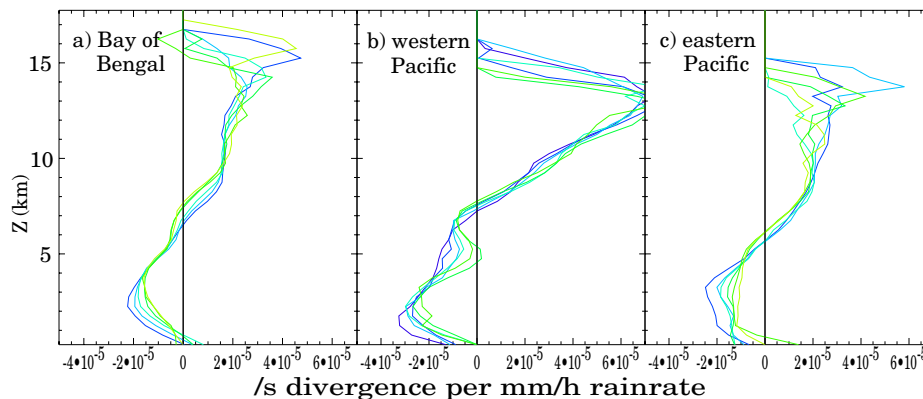

Fig. 4.1. Profiles of the regression coefficient between horizontal wind divergence estimates from Doppler velocity data and near-surface rainrate estimated from radar reflectivity, for 3 month-long radar deployments at sea. Profiles are shown from three approximately month-long deployments of shipborne Doppler radars in the Indian ocean (May 1999), west Pacific (Dec. 1992–Jan. 1993), and east Pacific ITCZ (July 1997).
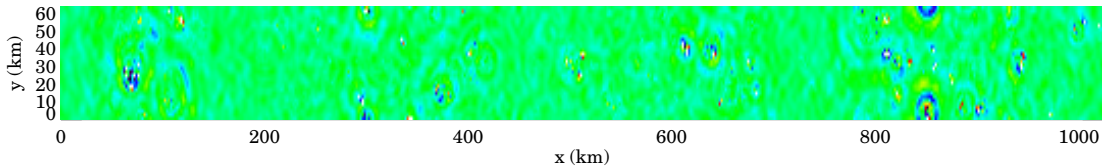
Fig. 4.2. Vertical velocity at 1500 m altitude in a doubly-periodic cloud-resolving model run. White patches (off the ends of the color scale) are convective updrafts (inside red regions) and downdrafts (inside blue regions).

tive updrafts and downdrafts (white patches) are clustered in certain preferred areas, all embedded in the context of a complex gravity wave field. Complete quantitative data about thermodynamics and microphysics as well as motion fields are available—far beyond the capabilities of observations. The simplified context of statistically steady states, periodic domains, and known governing equations allows parameterization hypotheses to be developed, tested, and refined in a tractable context.

More realistic model studies of convection are being pursued with a nested-grid strategy in a mesoscale model (the MM5). The finest grid can resolve convection, while coarser grids require a cumulus parameterization scheme, so this project spans the interface between resolved and parameterized convection. The information flow in the model is

very complex, rendering interpretation challenging, but the influence of complex, realistic lower boundary conditions on convection can be studied in detail.

Figure 4.3 shows simulated 3-hour rain accumulations over western Colombia and the adjacent eastern Pacific ocean on 3–4 September, 1998. This region is particularly interesting because it has both steep topography and a strong sea surface temperature gradient offshore, north of the equatorial cold tongue.

In the afternoon/evening, convection occurs over land, fueled by the accumulated moisture from many hours of strong surface fluxes and locally forced by a well-defined sea breeze front near longitude –76.5. In the late night and morning, by contrast, convection erupts in a mesoscale region offshore. Runs without topography suggest that this is due to a
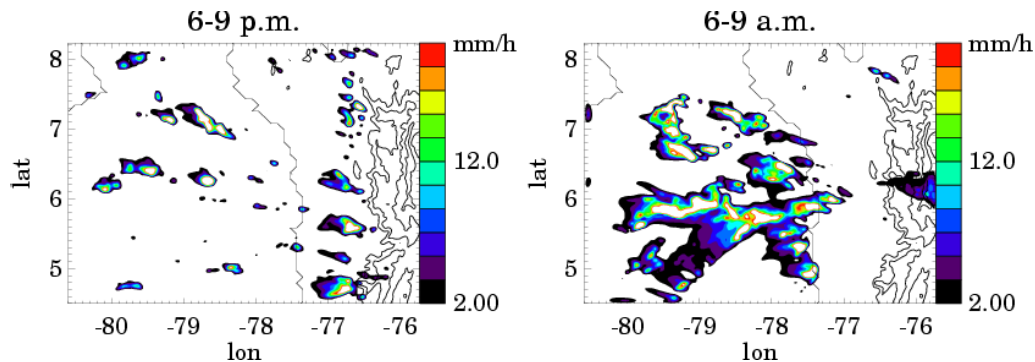

Fig. 4.3. Rainfall rate on 3–4 September 1998 in a nested domain of the MM5 model at 2 km grid spacing. The coasts of Colombia and Panama and 1 km and 2 km terrain elevations are indicated with open contours.
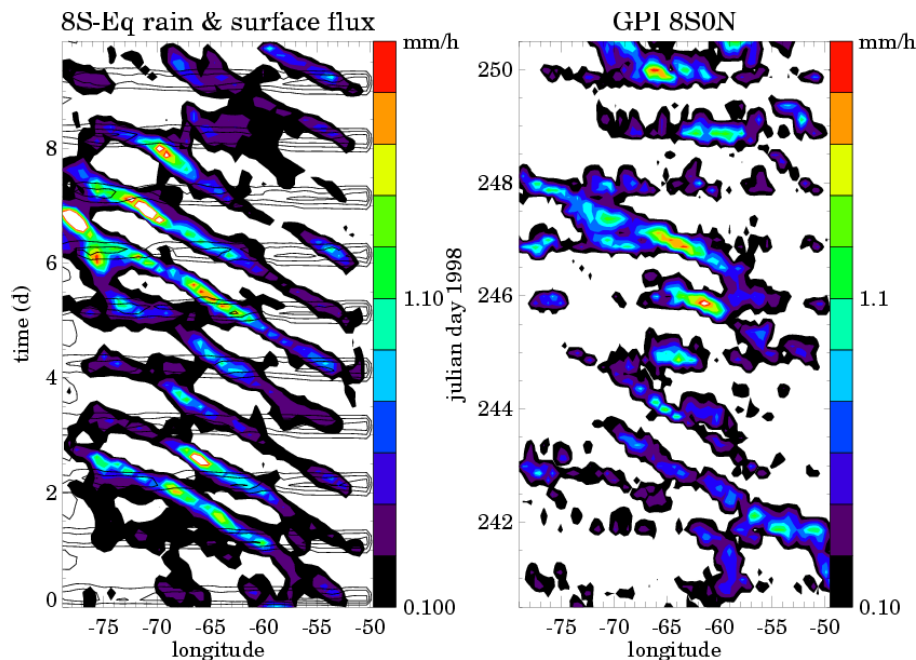
Fig. 4.4. Model (left) and satellite-observed (right) rainbands over the Amazon. Open contours are model surface flux, with contours at 200, 400, and 600 W m^{-2}.

mountain-lowland breeze, not a thermal land breeze *per se*.

The larger, coarser domains of the same model illustrate the interaction of parameterized convection, atmospheric dynamics, and a state-of-the-art land surface model of the Amazon basin at a 72 km grid spacing. Figure 4 shows time-longitude sections of rainfall (color) over the Amazon basin (8°S–Equator) during 28 August–7 September, 1998, from the MM5 (left) and satellite observations (right). Rainbands sweep across the basin, from eastern Brazil to the Andes, at 10 degrees per day.

While the surface fluxes are spatially coherent across the basin (driven by the solar input), the convection occurs in traveling bands, exhibiting some enhancement in the afternoon. The result

of this is that the long-term climatology of convection has a striped structure. If we think of the ultimate driver of convection as being the heating of the atmosphere from below, **Fig. 4.4** suggests that convection may be out of equilibrium with this driving by at least half a day, even over a hot moist continent.

These findings suggest that equilibrium parameterizations of convection, as are used in many prediction models, may be inadequate. To explore the consequences of cumulus parameterization assumptions, it is helpful to first consider more idealized large-scale models with parameterized convection. **Figure 4.5** shows rainfall patterns from one run of an idealized model on an earth-sized planet. A warm sea-surface temperature anomaly is specified in the middle of the picture, and the time-mean rainfall enhancement
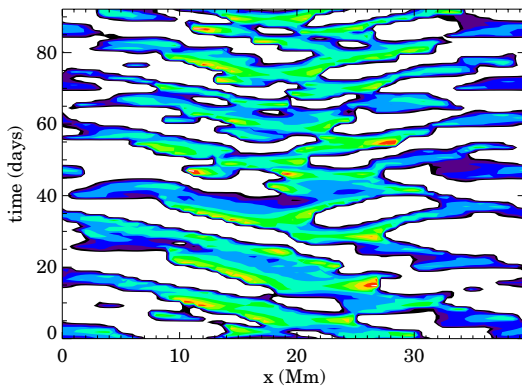
Fig. 4.5. Rainfall rate in an idealized model (Mapes 2000) with a sea surface temperature anomaly in domain center.

depends on the dynamics of the propagating transient activity, which in turn depends on aspects of the cumulus parameterization.

The broad perspective on convective variability afforded by the multi-model approach outlined above is being used to develop convective parameterization schemes whose behavior in models and whose spatial correlation statistics more closely mimic the observations. Models on the various spatial scales can then be used as testbeds for different cumulus parametrization schemes and hypotheses.

4.2 Clouds and Climate

Clouds have a large impact on radiative fluxes, impacting the net energy budget of the climate system, atmospheric heating rates, and energy exchange between the Earth's surface and the atmosphere. Cloud formation is organized by the large-scale atmospheric circulation and, in concert, cloud radiative forcing (CRF) is organized on large-scales. This makes clouds important both for dynamic circu-

lations within the climate system and for model errors that degrade climate simulations, weather forecasts, and reanalysis data. CDC has used observations of cloud variability (e.g., from ISCCP) in a variety of diagnostic and modeling studies in order to improve our understanding of the role of clouds in the climate system.

4.2.1 A high order statistical cloud scheme for GCMs

Large scale models such as those used for weather and climate prediction represent the state of the atmosphere at a discrete set of grid points. These values are used to determine the rates of various processes occurring within the grid cell (how much cloud water is converted to rain, for example). But atmospheric properties vary at all spatial scales, so the properties within a grid cell are better represented by some distribution instead of a single value. If process rates depend non-linearly on the quantity in question, the rate averaged over each grid cell may be different than the rate computed from the grid cell average. The problem is most acute in clouds, especially when computing precipitation rates, as these processes are strongly non-linear in the amount of condensate. The sub-grid scale homogeneity bias in process rates can easily be a factor of two, and is likely the reason models need to be arbitrarily re-tuned at each change in spatial resolution.

CDC and GFDL scientists are working on a statistical cloud scheme that will account for unresolved spatial variability

in the computation of process rates. Cloud resolving model simulations of convection over a mid-latitude land site are being used in two ways: to determine the distributions and parameters that best describe the variability in thermodynamic quantities that would not be resolved by a large-scale model, and to assess how these parameters change according to each physical process. **Figure 4.6**, for example, shows a time-height image of the standard deviation of total water content that would be computed from a model with 512 km grid size and 1 hour time step. Overlaid on this are contours of the detrainment from convective updrafts, which can be seen to increase the amount of variability.

The eventual goal of this work, funded by the Department of Energy through the Atmospheric Radiation Measurement program, is to implement a statistical cloud in the GFDL Flexible Modeling System that predicts higher order moments of one or more thermodynamic quantities at each grid cell. Such a scheme should require substantially less arbitrary tuning than current models, and should be insensitive to changes in spatial and temporal resolution.

4.2.2 A parameterization of cloud overlap for general circulation models

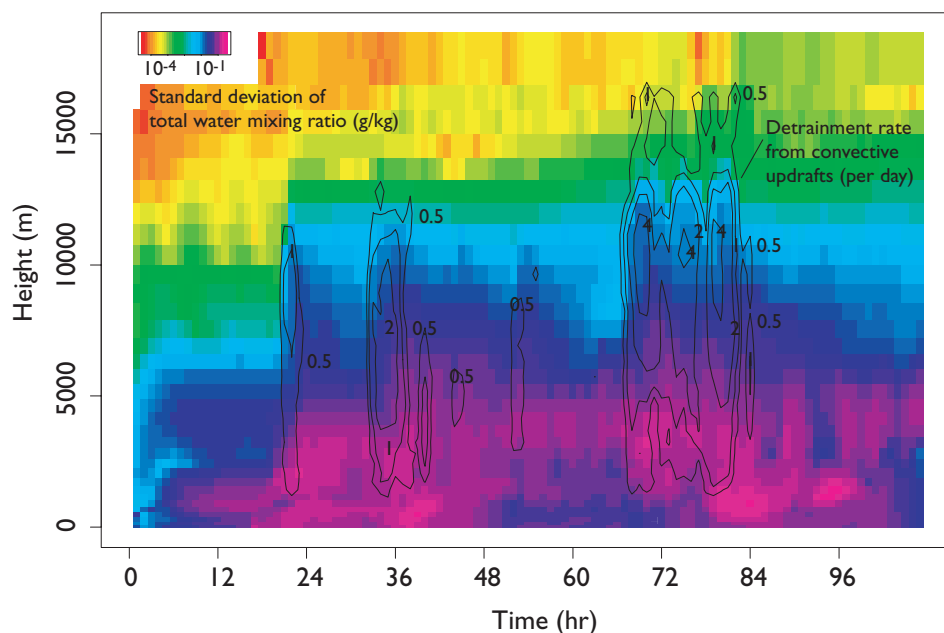How cloud overlap is specified in a general circulation model can have a large

Fig. 4.6. Time-height image of the variability in total water content that would not be resolved by a GCM. The standard deviation of total water (vapor, liquid, and ice) is computed from cloud resolving model simulations of vigorous convection over a continental land site with 2 km resolution sampled every 5 minutes. The small scale values are aggregated to 512 km and 1 hour time step at every level. Variability is in principle produced by turbulence, advection, microphysical process, and convection. The contribution of the latter is clear: the contours show detrainment from convective updrafts, which typically increase the amount of variability.

impact on radiative fluxes and heating rates. Current parameterizations of cloud overlap are also strongly sensitive to changes of vertical resolution. We have recently developed an overlap parameterization that is insensitive to changes of vertical resolution. In our scheme cloud overlap is described in terms of the correlation between horizontal cloudiness functions at different vertical levels. That correlation is assumed to decay exponentially with the separation distance between levels. This allows cloud overlap to be specified in terms of a single parameter, the decorrelation depth. While all pair-wise overlap fractions among cloudy levels can be calculated from the cloudiness correlation, those fractions can over-constrain the determination of the cloud distribution. It is found that cloud fraction in each level along with the overlap fraction among nearest neighbor cloudy levels is sufficient to specify the full cloud distribution. Our overlap parameterization has other desirable features that allow one to interpret the properties of complex cloud distributions in a simplified framework.

4.2.3 The seasonal cycle of cloud radiative forcing in the tropical Pacific

The radiative transfer model from NCAR's general circulation model CCM3 was modified to calculate monthly radiative fluxes and heating rates from monthly observations of cloud properties from ISCCP and temperature and humidity from ECMWF analysis. The modified model was efficient enough to allow a wide range of sensitivity tests. Seasonal variations of cloud radiative forcing were then investigated over the tropical Pacific. This quantifies the impact of clouds on atmospheric heating and on surface energy fluxes. The impact of CRF on surface winds, which also affect energy and momentum transfer at the surface, was then estimated in a linearized calculation of the tropical circulation forced by diabatic heating rates.

Typically, over the tropics, CRF represents approximately 20% of the annual variations of diabatic heating rates over convective locations and 50% or better at nonconvective locations. Seasonal variations of atmospheric CRF, when strong, tend to be in phase with those of total diabatic heating rates, indicating that clouds reinforce tropical circulations driven by latent heating. Cloud radiative forcing tends to have a stronger influence in the lower troposphere than at upper levels. It influences local circulations more than remote ones.

In the tropical east Pacific (85°W to 105°W), we investigated two mechanisms through which seasonal variations of CRF can impact seasonal variations of SST. The first is the 'direct' impact of CRF at the surface, which acts as an energy source for the upper ocean. The second is the 'indirect' impact of atmospheric CRF, which affects meridional surface winds that impact SST through coastal Ekman pumping that brings cool subsurface waters to the surface in the tropical east Pacific. CRF is a major contributor to the energy budget at the surface and in the atmosphere, particularly near and just south of the equator where seasonal variations of SST are strongest
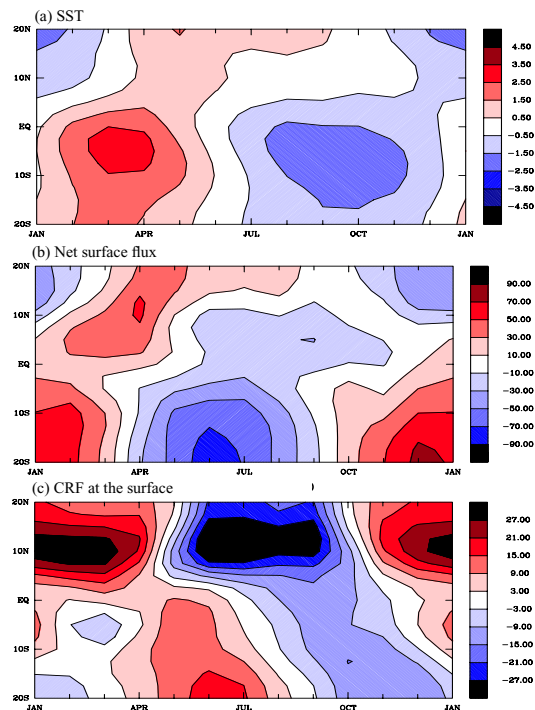
Fig. 4.7. The annual cycle of (a) SST, (b) net surface flux (W m^{-2}), and (c) cloud radiative forcing at the surface in the east Pacific.

(**Fig. 4.7a**). The amplitudes of seasonal variations of surface CRF (**Fig. 4.7c**) are

20–30% as large as those of the net surface flux (**Fig. 4.7b**). However, while the phase relationship between net surface flux and SST is consistent with the surface flux acting to force SST changes (i.e., surface fluxes lead SST by about 3 months), the phase of CRF is not consistent with it forcing SST changes. In fact, over locations where the seasonal cycle of SST is strongest, CRF tends to be out of phase with net surface fluxes, indicating that, if anything, the seasonal cycle of CRF damps SST variability. In contrast, the impact of CRF on meridional winds (relative to latent heating) is strong over the cold tongue (**Fig. 4.8**). Winds driven by CRF also have the correct phase to force the observed seasonal cycle of SST. So, to the extent that surface energy fluxes force the seasonal cycle of SST in the east Pacific, clouds are either unimportant or act to dampen SST variations. To the extent that upwelling driven by meridional winds is important, CRF, principally from season-
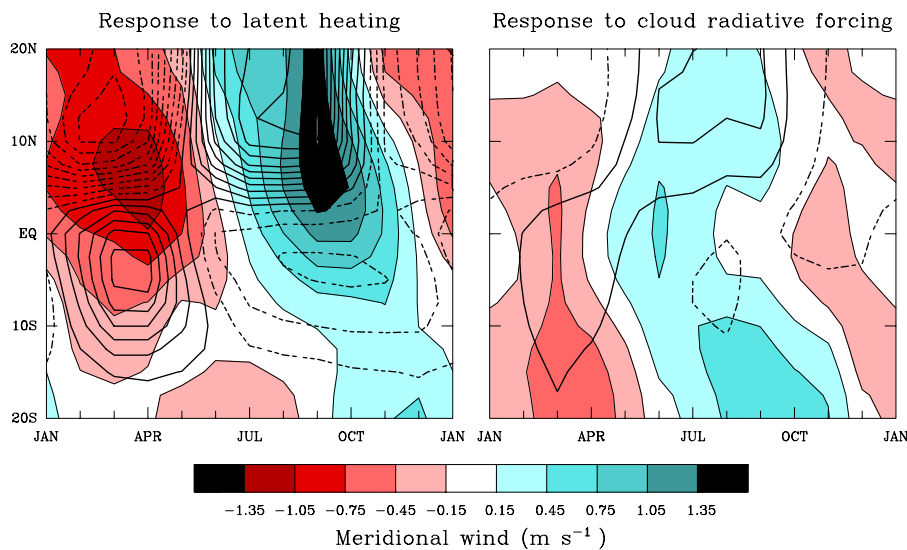

Fig. 4.8. The annual cycle of meridional surface winds calculated in a linearized atmospheric model from (a) latent heating and from (b) atmospheric cloud radiative forcing.

ally varying stratocumulus, is very important.

4.3 Studies of atmospheric angular momentum

Atmospheric angular momentum (AAM) provides a convenient framework to study the role of mountains, surface wind stresses and various transport mechanisms in variability ranging from intraseasonal to interdecadal and beyond. Quantitative studies are feasible with current global assimilated datasets which show a good budget balance for global integrals, intraseasonal variations and during northern winter/spring. The budgets get much worse when gravity wave drag is included, if zonal integrals are considered or during summer/fall seasons. AAM is useful as an index of the large scale zonal flow since it is highly correlated with independent length-of-day measurements and with phenomena such as the QBO, ENSO, the MJO and possibly global warming. CDC scientists have examined several aspects of AAM variability, including: the link to MJO tropical convection, a linear model of global AAM and its torques, the global AAM budget imbalances due to gravity wave drag, the forcing for the semiannual seasonal component of AAM and the AAM response to global warming in an ensemble of coupled ocean-atmosphere model runs. CDC also monitors in real time the complete vertically integrated budget as part of its web-based maproom activities and distributes AAM and torque data to other researchers.

4.3.1 The Madden-Julian oscillation

A composite study of the MJO AAM signal was performed using 30–70 day filtered data and global AAM tendency as a linear regression "predictor". Large-scale eddies forced by tropical convection were found to play a dominant role in forcing the AAM response during northern winter (November-March). As these eddies move eastward within the asymmetric basic state, they produce a poleward movement of momentum transports. When this upper tropospheric momentum source reaches the subtropics, it induces a vertically deep mass circulation and a subtropical friction torque anomaly, which causes AAM to change. For the mountain torque, a combination of equatorial Kelvin waves, forced by convection over Indonesia and then impinging on the Andes and mass exchanges along the east slopes of the Himalayas and Rockies were found. The former is more directly linked with the MJO while the latter is a residual of large amplitude, ubiquitous torques induced by mid-latitude synoptic wavetrains. In fact, a case study of an individual MJO, where the mountain torque was 3x larger than the frictional torque, prompted a linear model investigation of the torques and their role in forcing intraseasonal AAM anomalies.

4.3.2 A linear model of global AAM

A simple Markov model of the three-component system comprised of total AAM, friction and mountain torque was developed. Statistical analysis of the observed data suggested AAM anomalies
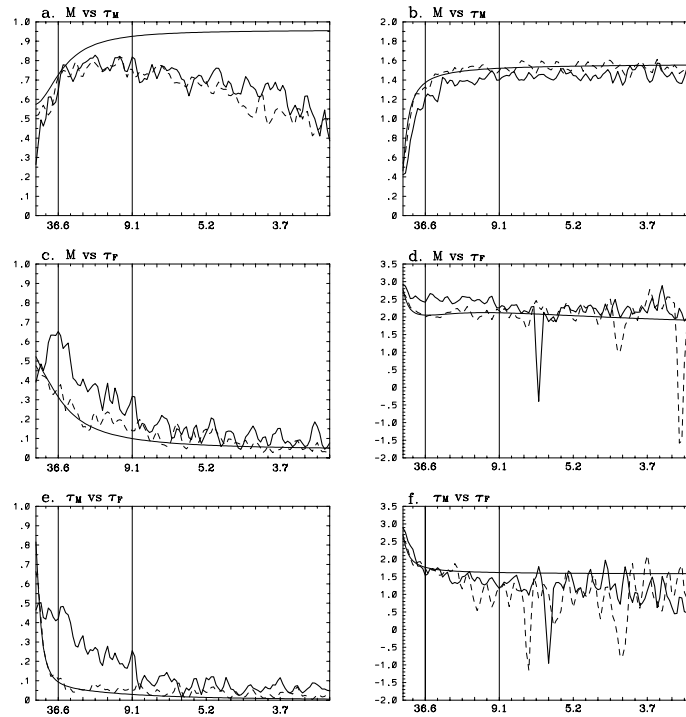
Fig. 4.9. Coherence squared (left column) and phase (right column) between the variables labeled at the top of each panel. Three curves are shown in each panel: the thick solid lines are for the observations, the smooth curves are the theoretical cross spectra and the dashed lines are based on output from a red noise model. The coherence squared and phase (in radians) are plotted as a function of Fourier frequency (cycles/366 days) with selected labels along the abscissa showing the corresponding period in days. A positive phase means the first variable labeled above each panel lags the second variable

are damped on a 30 day time scale by the friction torque and forced stochastically by a "white" mountain torque and a "red" friction torque. The resulting Markov model has variances and lagged covariances that compare favorably to the observations, although systematic differences representing approximately 20–30% of the variance also emerge (see **Fig. 4.9**). The most prominent differences are the greater coherence between the mountain and friction torque for 10–90 day periods in the observations (see **Fig. 4.9e**) and the excessive AAM variance at $\sim 2\pi * 30$ days (the AAM decay time scale) in the modeled spectrum (not shown).

About 30% of the torques' variance in the 10–90 day band is coherent in the observed data versus <10% in the Markov model. In both the observations and the model, the friction torque leads the mountain torque. Physically the relation reflects primary forcing of AAM by the mountain torque and primary damping by the friction torque. It occurs weakly in the Markov model because the 30 day damping on AAM is "assigned to" the friction torque. For the MJO the same relation accounts for ~45% of the variance. The increase appears related to the timing of the torques' response to tropical convective forcing and adds to a background coherence, as given by the

Markov model. When linear inverse modeling is performed that accounts for feedback among the variables, the modeled AAM spectrum is improved somewhat and the skillful prediction of AAM is extended by 2 days.

The differences that remain after accounting for the linear feedbacks may be tied to limitations imposed by analyzing the global integrals. This naturally leads to three degrees-of-freedom for the simple Markov model which may be insufficient to describe the system accurately over a broad frequency range. In particular, the 30-day decay time scale for AAM blends interannual and intraseasonal variations that include both oscillatory and damped modes. Further improvement in the linear model requires analysis of a more complete set of variables that include deviations from the global mean.

4.3.3. Global torques and regional synoptics

The synoptic features associated with global mountain and frictional torques were also studied. The primary synoptic structure producing the mountain torque during northern winter is seen in **Fig. 4.10**. Growth of quasi-geostrophic disturbances upstream of the mountains is followed by downstream dispersion of energy across the mountains. At the surface, mass anomalies propagate southward, likely reflecting topographic Rossby wave activity forced by low level flow impinging on the mountain slopes. Zonal mean momentum anomalies produced by the torque are transported out of the latitude band of the mountain. This is accomplished partially by the quasi-geostrophic wave activity. The momentum is dissipated in adjacent latitude bands by the friction torque which responds to the upper level momentum source produced by the transports. The mass anomalies are consistent with quasi-geostrophic balance of the surface flow. The decay time scale of the global mountain torque is ~1.5 days, i.e., it is nearly white for daily data.

Synoptic developments are more complicated with the global friction torque which has a slower, 6 day decay time scale. Such low frequency forcing implies larger AAM anomalies and possibly enhanced predictability. Regression, using the global friction torque as a "predictor", reveals zonal mean momentum transports across 35°N during northern winter can initiate intraseasonal growth and decay of AAM anomalies. **Fig. 4.11** shows the composite evolution of 250 mb streamfunction and SLP anomalies when regressed on the friction torque. The streamfunction pattern at day −10 (**Fig. 4.11a**) has a ring of anticyclonic centers along 30–40°N, consistent with northward momentum transports across 35°N. The sequence which follows (**Figs. 4.11b-d**) shows wavetrains amplifying over east Asian and then North American orography, low pressure moving equatorward east of these mountains and pre-existing zonal mean easterly wind anomalies south of 35°N intensifying (**Fig. 4.11c**, mountain torque < 0) and then weakening (**Fig. 4.11d**, friction torque > 0).
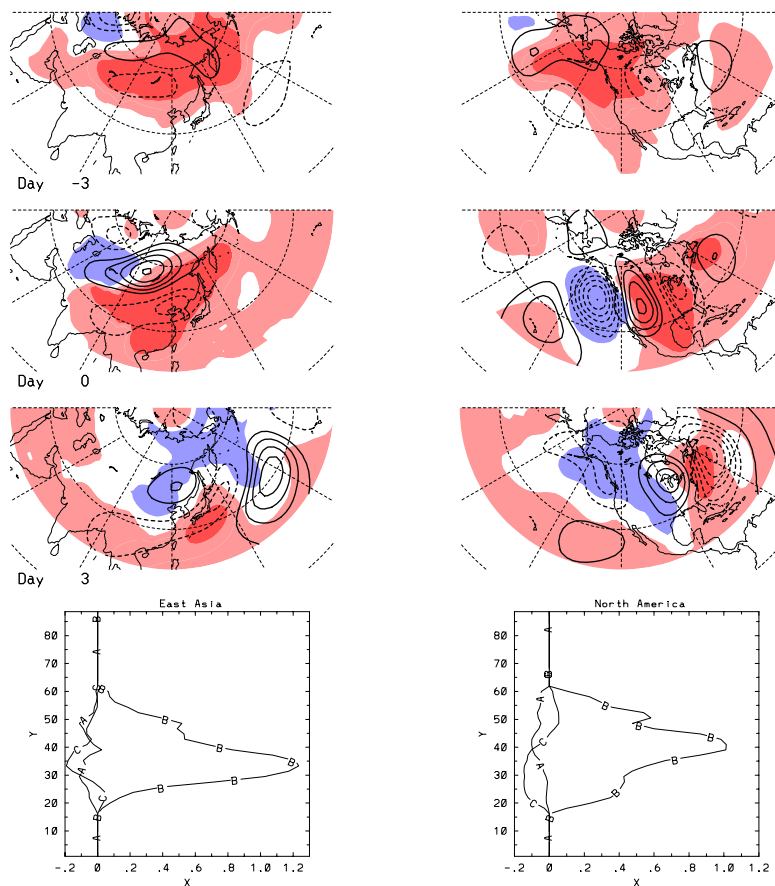
Fig. 4.10. The 250 mb streamfunction (contours) and sea level pressure (shading) anomalies that accompany a mountain torque over Asia (left column) and North America (right column) at days –3, 0, +3. The fourth panel in each column shows the mountain torque (Hadleys) as a function of latitude for each day. The curves labeled A, B and C correspond to days –3, 0 and 3 respectively.

The negative zonal mean mountain torque at days –2 to –6 is balanced by momentum transports that produce a momentum source in the orographic regions and a momentum sink in adjacent regions (or latitude bands). The atmosphere responds with easterly surface wind anomalies as it adjusts to the momentum sinks and these are supported geostrophically by lower pressure in the tropics and higher pressure in the extratropics (e.g., **Fig. 4.11c**). The mass and wind fields are especially strong over the Pacific sector where the 250 mb pattern projects onto the PNA. The positive friction torque counteracts the negative AAM tendency produced by the mountain torque leading eventually to a weak positive AAM anomaly. The 6-day decay time scale for the friction torque translates to a typical life cycle of an event lasting ~30–40 days. The close proximity to the MJO oscillatory time scale of 30–60 days suggests a good chance for interaction and feedback, both through the tropical convection and through the momentum and heat transports.
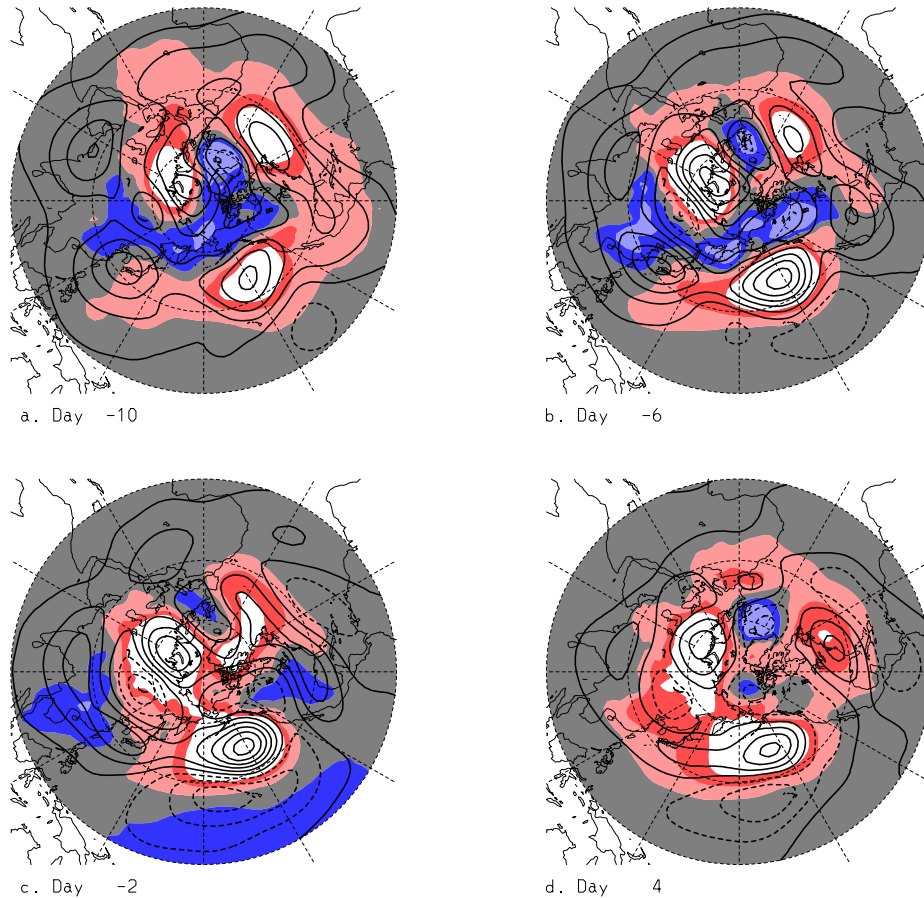
Fig. 4.11. The evolution of 250 mb streamfunction (contours) and sea level pressure (shading) anomalies that accompany the global frictional torque: a) Day –10, b) Day –6, c) Day –2 and d) Day +4. The red and white shading highlights positive SLP anomalies while the blue and gray shading highlights negative SLP anomalies.

4.3.4 Balance of global angular momentum in reanalysis data sets

The long-term balance of global angular momentum was examined in the NCEP reanalysis data set. In a perfect balance, the tendency of global atmospheric angular momentum should equal the total surface torque that comprises the three components of the mountain (T_M), friction (T_F), and gravity wave (T_G) torques. The gravity wave torque arises from the parameterization of subgrid-scale orographic gravity wave drag in the NCEP reanalysis model. Because T_F and T_G are not constrained by observation, a budget imbalance in the reanalysis data may exist. The extent of this imbalance reflects the realism of the assimilated data set. An extensive budget analysis of the NCEP data revealed a significant imbalance of angular momentum, on the order of −10 hadleys (negative value indicates that the torque is less than the tendency of angular momentum) for the annual mean. This imbalance is caused mainly by the gravity wave torque, as a removal of T_G reduced the annual-mean

budget imbalance to −2 Hadleys. More-over, the greatest imbalance occurs in winter, when the magnitude of T_G reaches its maximum. **Figure 4.12** shows the seasonal and annual mean budget imbalance with (red) and without (blue) T_G. The budget imbalance in the reanaly-sis data strongly suggests deficiencies in the T_G parameterization scheme that may cause a loss of global angular momentum in real forecasts made with the NCEP GCM. This point was immediately con-firmed by examining an extensive set of 8-day forecasts made with the NCEP reanalysis model. The rate of loss of glo-bal angular momentum in these medium-range forecasts is on the same order of magnitude as the budget imbalance deduced from the reanalysis data. These results constitute a critical examination of the realism of the NCEP reanalysis data. They also point to the potential neg-ative impact of the gravity wave drag on numerical weather/climate prediction. Finally, the T_G in the ECMWF reanalysis data is very similar to its counterpart in the NCEP reanalysis in its magnitude and temporal variability. It is very likely
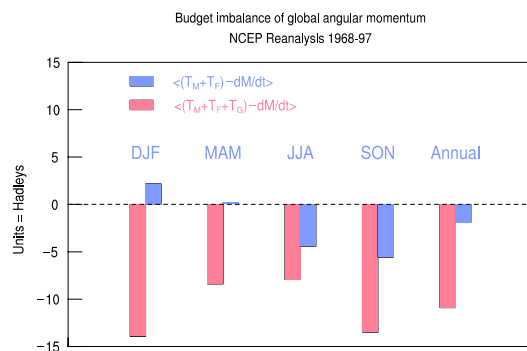
that the same problem of budget imbal-ance of angular momentum, caused by T_G, also exists in the ECMWF reanalysis data and the ECMWF GCM.

4.3.5 Impact of parameterized gravity wave drag on GCM weather/climate pre-diction

This study was inspired by the budget analysis of global angular momentum described above. After finding the poten-tial problem with the orographic gravity wave drag (GWD) in degrading the bal-ance of global angular momentum, the impact of GWD on weather/climate pre-diction was examined by performing a series of extensive GCM simulations with varied strength of GWD. The GCM used was a recent version of the NCEP global forecast model. The numerical experiments comprised 9 sets of medium-range (2 week) forecasts, each using a different value of the surface GWD parameter ranging from 0 (no GWD) to 2 x GWD (twice the standard value used in the original NCEP model). Each set of forecasts, in turn, consisted of 20 runs from a series of initial condi-tions 5 days apart from the 1997–98 win-ter. The results showed a clear degradation of the forecasted global angular momentum as the strength of GWD increases, consistent with our pre-vious budget analysis. At the same time, GWD did provide some improvement in the forecast of the local zonal mean angular momentum in the midlatitude of the Northern Hemisphere, a characteris-tic that has been emphasized by propo-nents of GWD parameterization.

Fig. 4.12. The budget imbalance of global angular momentum for seasonal and annual means, based on NCEP reanalysis data from 1968–1997. The imbalance estimated with and without gravity wave drag are shown in red and blue. Units in hadleys.

Thus, increasing the GWD in the model introduces opposite effects in the errors of the global and local angular momentum. This is most clearly illustrated in **Fig. 4.13a**, the forecast error of global angular momentum (filled circles) and the area-weighted RMS forecast error of local angular momentum (open circles) for the Northern Hemisphere as functions of the GWD parameter. Each circle represents the error at day 10 averaged over 20 forecasts. **Figure 4.13b** is similar to **Fig. 4.13a**, but with the error normalized by the grand average across the nine parameter values of GWD. The robustness of the result is demonstrated by the smallness of the difference between the 20- (black) and 10- (red) forecast averages. The detailed structure of the local forecast error of zonal mean zonal wind as a function of the GWD parameter was

investigated. It is found that in the absence of GWD the forecasted zonal wind is too strong in the midlatitude but too weak in the subtropics of the Northern Hemisphere. The two local errors partially cancel each other such that the error in the global angular momentum appears to be small. The effect of GWD is to partially reduce the local error in the N.H. midlatitudes without affecting other areas. Thus, the stronger the GWD, the greater the negative bias in the forecasted global angular momentum. These results indicate that the GWD parameterization scheme is not consistent with the balance of global angular momentum. Research into alternative parameterization schemes for the mechanical dissipation in the GCM that is capable of correcting both local and global errors of angular momentum in the same direction is warranted.
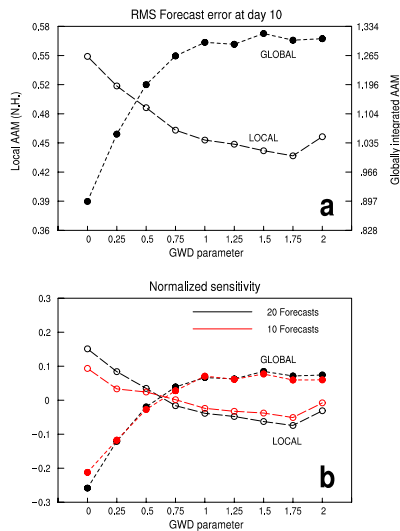
4.3.6 Annual and semiannual cycles of atmospheric angular momentum

The mechanism for the semiannual oscillation of atmospheric angular momentum was examined. Upper-tropospheric winds, whose angular momentum is an excellent proxy of the vertically-integrated angular momentum, were used. The observed seasonal cycle of the zonal wind or angular momentum is dominated by its first two (annual and semiannual) harmonic components (**Fig. 4.14, top panel**). The seasonal variation of the rotational component (the part that contributes to global angular momentum) of the upper-level winds was diagnosed in a nonlinear upper-tropospheric vorticity-equation model with specified diver-

Fig. 4.13. (a) The forecast errors of global relative angular momentum (filled circles) and local angular momentum (open circles) at day 10, averaged over 20 forecasts, as functions of the GWD parameter. Units in AMU (1 AMU = 10^{25} kg m^2 s^{-1}). (b) Same as (a), but normalized by the average of all nine points in each curve. Red curves are the errors deduced from 10 forecasts.

gence (Rossby wave source) and transient eddy forcing. The divergence forcing is the more important of the two, especially in the Tropics and subtropics, where it is associated with tropical heating and cooling. Given the harmonics of the forcing, the model predicted the harmonics of the response, that is, the vorticity, from which the harmonics of angular momentum can be calculated. This procedure itself is an innovative way of diagnosing a temporally periodic phenomenon. It can, in principle, be generalized to the three-dimensional atmosphere or a coupled atmosphere-ocean system. The surprising but clear conclusion from our diagnosis is that the semiannual harmonic of atmospheric angular momentum arises more as a nonlinear response to the first (annual) harmonic of divergence forcing than as a linear

response to the second harmonic of divergence forcing. To illustrate, the bottom panel of **Fig. 4.14** shows the response of global relative angular momentum (first three harmonics) to a specified divergence forcing that contained only the annual mean plus the first harmonic. In this case, in the complete absence of a second-harmonic forcing, the second harmonic response resembles that observed in both amplitude and phase. Another case with specified second harmonic (but not first harmonic) forcing failed to produce a realistic response in the angular momentum. Thus, the semiannual harmonic of solar radiative forcing arising from the sun crossing the equator twice a year may not be as important as previously thought in generating the semiannual cycle of atmospheric angular momentum. The result is a clear demonstration that external forcing at one frequency can produce primary atmospheric response at a different frequency. Since it has been shown previously that significant errors exist in the semiannual harmonic of angular momentum or zonal wind in GCM simulations, the findings point to the possibility that these errors may be related to the first harmonic of the radiative/diabatic forcing as well as the detailed treatment of the interaction between this forcing and the annual harmonic of the tropical circulation.

4.4 Air-sea interaction related to the MJO

There is growing interest in the role that air-sea interaction may play for the dynamics of the Madden-Julian oscilla-
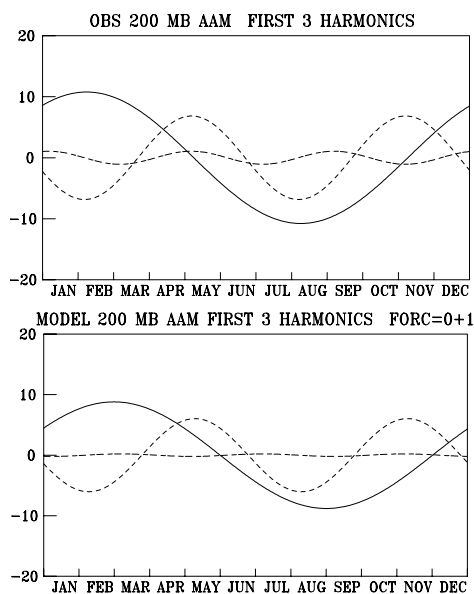

Fig. 4.14. The observed (upper) and model simulated (lower panel) first three harmonics of relative angular momentum at 200 mb. In the simulation only the annual mean and first harmonic of divergence forcing are applied to the vorticity equation model.

tion. Such interest has been motivated by the poor performance of GCMs in simulating and forecasting the MJO. Models with prescribed SST typically produce MJOs that move eastward too fast, are too weak, and have incorrect seasonality. Field programs, such as TOGA COARE, have revealed local swings in SST in excess of 1°C in association with passage of the MJO across the warm pool of the Indian and western Pacific Oceans. The forcing and importance of these anomalies both within the MJO cycle itself and as a link with low frequency variations are subjects of CDC research.

4.4.1 The MJO cycle

Comparison of the observed SST tendency and the net surface heat flux into the equatorial western Pacific indicates that surface heat flux forcing by the MJO is likely responsible for the observed intraseasonal SST variations. A detailed study of the surface heat fluxes associated with the MJO indicates the dominance of short wave radiation and latent heat flux. The structure of the MJO is such that minimum surface short wave radiation occurs just prior to maximum latent heat flux. Thus these two fluxes act in concert to cool the ocean after the passage of the convective-windy phase of the MJO. Similarly, increased short wave radiation and reduced latent heat flux act to warm the ocean during the clear-calm phase of the MJO.

The dominance of one dimensional processes for controlling the SST variations associated with the MJO has been demonstrated using a grid of one-dimen-

sional mixed layer models. Each grid was forced with observed surface fluxes for 10 well-defined MJO events. The composite of model output (not shown) indicates that surface heat flux forcing is responsible for the observed intraseasonal SST variations across the equatorial Indian and western Pacific Oceans. This result is at odds with point measurements made during TOGA COARE, which suggests a significant role for horizontal advection. This issue was addressed by repeating the mixed layer model experiments using an Ocean GCM. Again, the observed intraseasonal SST variation produced by the composite MJO was simulated. But, analysis of the role of horizontal advection (**Fig. 4.15**) emphasizes the dominance of surface heat flux forcing. While horizontal advection is locally large (as in TOGA COARE), it is incoherent on the scale of the MJO.

The potential impact of intraseasonal SST anomalies, induced by the MJO, on the dynamics of the MJO was investi-
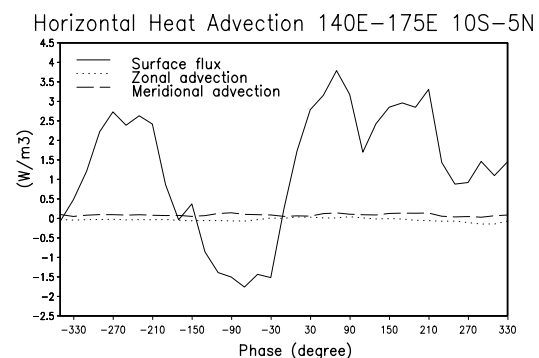

Fig. 4.15. Composite area average (140°E–175°E, 10°S–5°N) zonal (dotted line) and meridional (dashed line) heat advection (W m^{-3}) of upper 10 m and the surface heat flux divided by 10 m (thick line). Positive values indicate warming.
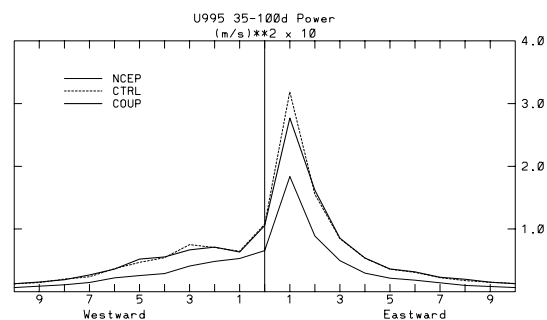
Fig. 4.16. Wavenumber spectra for the surface zonal wind from the NCEP-NCAR reanalysis (thin curve), the control run (dashed curve), and the coupled run (heavy curve). Power was integrated for periods 35–90 days and averaged for each latitude between 15°N and 15°S.

gated in a GCM coupled to a grid of one dimensional mixed layer models. Simulating the ocean with a mixed layer model is appropriate for this study, as indicated by the above heat budget studies. In the particular GCM used for this study, coupling to an active mixed layer had very little impact on the model's MJO (**Fig. 4.16**). Unfortunately, due to a poor simulation of the surface structure of the MJO, the model was unable to reproduce the observed coherent eastward propagation of SST. The poor simulation of the surface structure of the MJO stems from both a poor simulation of the mean climate of the warm pool and an improper phasing of short wave radiation and latent heat flux. Thus, it remains an interesting question as to the role of intraseasonal SST anomalies for the dynamics of the MJO, and, for instance, whether prediction of intraseasonal SST is necessary for successful prediction and simulation of the MJO.
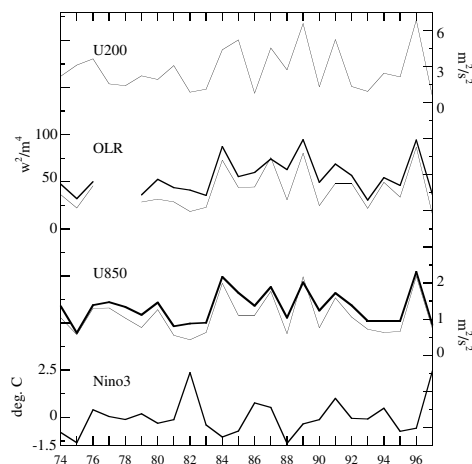

Fig. 4.17. Time series of (top to bottom) $[u_{30\text{-}90d}]^2$, $[OLR^2_{EOF}]$ (dark curve) and $[OLR^2_{EWVS}]$, $[U^2_{EOF}]$ (dark curve) and $[U^2_{EWVS}]$, and Niño3 SST averaged during Nov.–Mar. The units for OLR variance (on left) are $W^2\,m^{-4}$, for zonal wind variance (on right) are $m^2\,s^{-2}$, and for Niño3 SST (on left) are °C.

4.4.2 Interannual variation of MJO activity

The level of MJO activity in the Tropics is observed to vary widely from year to year. Understanding this interannual variability is of practical importance because of the role the MJO plays in the Australian and Indian summer monsoons, in forcing oceanic Kelvin waves that dominate the variability of the thermocline in the equatorial eastern Pacific, and the possible role that the MJO may play in the onset and evolution of ENSO. A detailed analysis of the interannual variability of the MJO during winter reveals little relationship between the overall level of activity and SST, including the state of ENSO (**Fig. 4.17**). Recent analyses of ensembles of GCM experiments have arrived at the same conclusion: most of the year-to-year variability of the level of MJO activity during win-
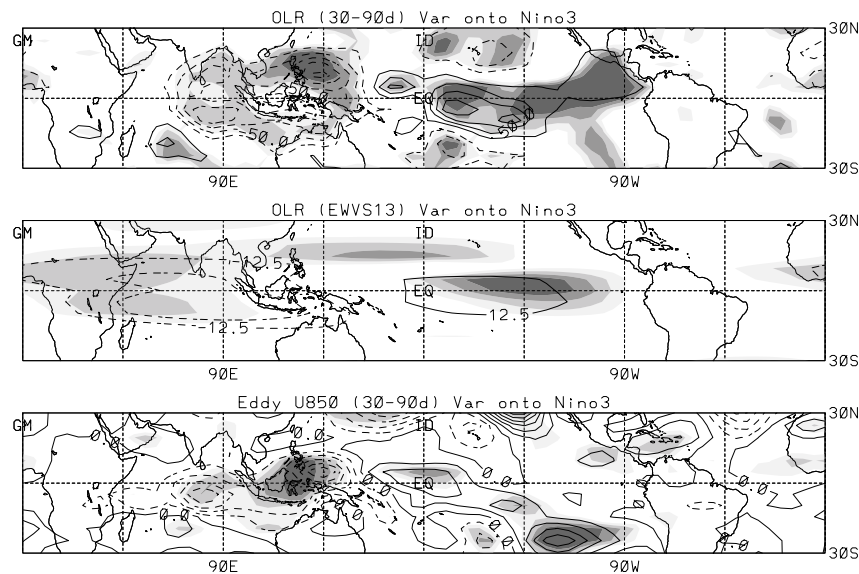
Fig. 4.18. (a) Regression of Nov.–Mar mean 30–90 day filtered OLR variance onto Niño3 SST. (b) Regression of OLR$_{EWVS}$ onto Niño3 SST. (c) Regression of 30–90 day filtered 850-mb zonal wind variance on Niño3 SST.

ter is unrelated to boundary forcing and is thus unpredictable.

On the other hand, MJO activity is observed to shift eastward during El Niño (**Fig. 4.18**). This eastward shift may have important dynamical consequences, especially at the onset of warm events. Furthermore, while the contemporaneous correlation between wintertime (DJFM) west Pacific SST and wintertime global MJO activity is small, there is a strong correlation when west Pacific SST leads MJO activity by 1 season. **Figure 4.19** shows a scatter plot of MJO activity in winter versus SST anomaly averaged over the west Pacific in the northern fall (SON). The lag correlation depicted is consistent with the synoptic observation that an expanded warm pool promotes strong MJO activity. The weak contemporaneous correlation in winter reflects the cooling effect of enhanced

MJO activity on local SSTs. Warm west Pacific SSTs also precede the onset of El

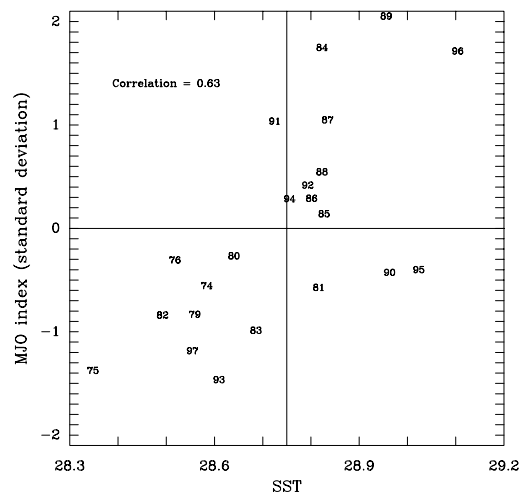**Fig. 4.19**. Northern fall mean SST (°C) plotted against MJO variance averaged over the following winter. Values have been averaged over 130°E–180°E, 15°S–15°N. MJO variance is calculated from the spectral power of eastward propagating zonal wavenumbers 1–6 and periods 35–90 days. The variance of each season has been normalized by the standard deviation of wintertime variances between 1974 and 1997.

Niño, which might lead one to infer a relationship between strong MJO activity and the onset of El Niño. However, of the three winters with the strongest MJO activity, only the winter of 1996–97 (year 96 in the figure) preceded a strong El Niño.

4.4.3 MJO and ENSO

Previous studies have suggested that intraseasonal variations of convection contribute to interannual variations in the tropical Pacific by acting as a triggering mechanism for El Niño. This speculation has increased recently because the 1997–98 El Niño, arguably the strongest of the century, followed exceptionally strong MJO activity during the winter of 1996–97. During the winter of 1996–97 there were two strong MJO events that could have contributed to the evolution of the 1997–98 El Niño. The first occurred during December 1996 and was accompanied by substantial cooling of the west Pacific, initiating a long-term cold anomaly there. The second occurred during February–March 1997 and was accompanied both by cooling in the west Pacific and warming in the central Pacific. The warming in the central Pacific was particularly important. After that warming, central Pacific SSTs remained warm for the next year and convective activity migrated to the central Pacific, signaling the onset of a very strong and rapidly developing El Niño. To help elucidate the potential role of MJO activity for the onset of El Niño, dynamical interactions were examined in the upper ocean that led to the important SST changes in the winter of 1996–97.

SST fluctuations that occurred in the west Pacific (**Fig. 4.20a**) during convective episodes in December 1996 and February 1997 (shaded periods) were, for the most part, forced by surface flux variations (**Fig. 4.20b**). Surface cooling was initiated by the reduction of SW surface fluxes due to enhanced cloud cover. Later, evaporative cooling during eastward wind anomalies reinforced that cooling. In February 1997, temperature advection (**Fig. 4.20c**) by ocean currents was also important for the SST perturbation; off-equatorial upwelling, through an anomalously large vertical temperature gradient, contributed substantially to west Pacific cooling.

During late March and early April 1997, central Pacific SSTs (**Fig. 4.20d**) warmed in response to an oceanic Kelvin wave that was forced during the February MJO. That warming was primarily due to zonal temperature advection (**Fig. 4.20e**), promoted by strong eastward currents along with an east-west temperature gradient. After the passage of the Kelvin wave, zonal currents remained slightly eastward because trade winds (**Fig. 4.20f**) did not resume their pre-Kelvin wave strength. In addition, the east-west SST gradient was reduced after the Kelvin wave. As a result, temperature advection was negligible after the Kelvin wave, and SST continued to warm due to the positive surface heat flux that is typical for the region. The zonal current variation that is responsible for the temperature advection is forced, in part, by a local wind-stress fluctuation. So, if the MJO did contribute to this important SST warming through nonlinear interac-
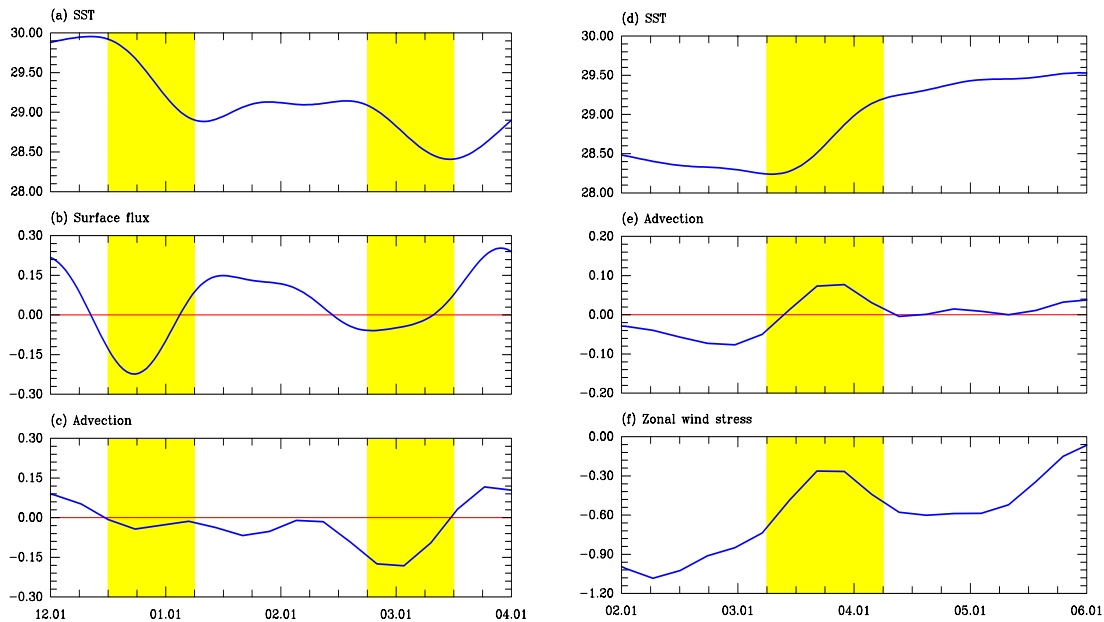
Fig. 4.20. SST and upper-ocean quantities averaged over the top 50 m. On the left are shown values in the west Pacific (10°S–10°N; 130°E–150°E) for December 1996 through March 1997 of: (a) SST (K), (b) net surface heat flux (K week^{-1}), and (c) temperature advection by ocean currents (K week^{-1}). On the right are shown values in the central Pacific (10°S–10°N; 160°W–180°W) for February through May 1997 of: (d) SST, (e) temperature advection by ocean currents (K week^{-1}), and (f) zonal wind stress (dyne cm^{-1}). Shaded regions indicate time periods of rapid SST changes.

tions, then those interactions involve the coupling of atmospheric and oceanic dynamics.

4.5 The South American Program

A large dataset of daily rainfall observations over South America culled from sources in several countries has allowed an examination of precipitation patterns on that continent with unprecedented spatial and temporal resolution. A comparison with rainfall estimates from other datasets that employ a combination of satellite and some gauge data has shown that the two estimates generally are within 10% of the rain gauge only estimates at 2.5° resolution for climatologies of a season or more. On the other hand, at some locations within the Amazon,

estimates of the annual cycle of rainfall from gauge observations and outgoing longwave radiation are several months out of phase.

4.5.1 Seasonal rainfall relation with SST

Interannual variability of seasonal rainfall in the Brazilian Amazon basin has been studied in the context of its relationship to sea surface temperatures in the tropical Pacific and Atlantic oceans. Simultaneous linear correlations reveal strong relationships, but the rainfall patterns are of regional scale.

With a few exceptions, the largest (absolute) correlations between 3-month seasonal rainfall and SST are found during the season of transition between wet and

dry or between dry and wet regimes. In a few cases there are large simultaneous correlations entirely within the dry season, but large correlations are never found entirely during the wet season. In the Pacific, large correlations are always confined to the eastern equatorial region, and warm SSTs are always associated with a deficit of rainfall. In the Atlantic, correlations are usually positive, and centered in the near-equatorial southern ocean.

It is hypothesized that during the transition seasons an important contributor to the SST control on seasonal totals is its influence on the timing of the rainy season onset or end. That influence appears to be stronger than the SST influence on the rainy season rain rate. This is illustrated by **Fig. 4.21**. **Figure 4.21a** shows the simultaneous correlation between April-June rainfall in the eastern equatorial Amazon and SST. The area chosen for the rainfall average is somewhat unusual in that it exhibits large correlations with both proximate oceans. When the ending date of the same area average of rainfall (with a climatological ending date of 13 June) is correlated with SST (**Fig. 4.21b**) the pattern that emerges is similar and of the same sign, suggesting that in this region the SST role in the timing of onset plays a role in the SST relationship with seasonal total rainfall. Further, when SST is correlated with the rainy season rate of rainfall (defined as the average daily rainfall from 1 April to the annually varying end of the rainy season), only weak correlations are evident (**Fig. 4.21c**). Thus it appears that the most important influence of SST in
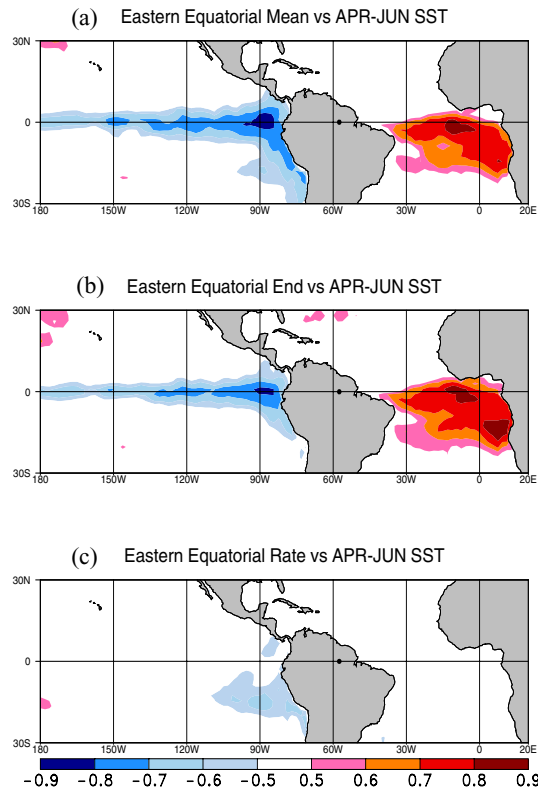

Fig. 4.21. Correlation between April-June SST and (a) April-June mean rainfall in eastern equatorial (average of 20 stations from 2.5°S–2.5°N, 60°W–55°W) Amazon, (b) eastern equatorial rainy season ending date, and (c) far eastern rain rate calculated from 1 April through end of rainy season. Included are years 1976–1997.

determining calendar season total rainfall is through its influence on the timing of the rainy season, rather than on the intensity of rainfall during the rainy season itself.

A battery of atmospheric general circulation models presently are being tested to determine whether these models produce a realistic onset over monsoonal South America when forced by realistic and evolving SSTs. The observed skill these models exhibit in simulating seasonal anomalies over equatorial South America also is being evaluated to determine

the role of model onset in contributing to that skill.

4.5.2 Intraseasonal variations in the SACZ

Mechanisms associated with subseasonal rainfall variability in the South Atlantic convergence zone (SACZ) have been examined. The SACZ arguably is the most important meteorological feature of South America, because it exhibits large variability at many time scales and its mean position passes over the most densely populated Brazilian states of São Paulo and Rio de Janeiro.

Correlations between submonthly (2–30 day band-pass filtered) OLR in the vicinity of the SACZ and 200 mb streamfunction reveal the preferred path of wave energy impinging on the SACZ to be Rossby waves from the midlatitudes of the Southern Hemisphere. Episodes of enhanced convection within the SACZ, indicated by negative OLR anomalies, occur at the leading edge of upper-level troughs propagating into the region. The corresponding pattern at 850 mb reveals that the disturbances are nearly equivalent barotropic west of South America, but tilt westward with height in the region of the SACZ. Negative low-level temperature anomalies lie to the southwest of the convection. The results are consistent with baroclinic development along an associated cold front. It also appears that the SACZ forms when the northwesterly flow associated with a low-level trough is able to tap moisture from the Amazon.

4.5.3 Climatology of extreme precipitation events

The climatology and interannual variability of heavy, or 'extreme', precipitation events in the state of São Paulo, Brazil were studied. An extreme event is counted at each station when daily rainfall exceeds a certain percent of its seasonal or annual mean. It is found that they occur mainly from November–March (the season during which the SACZ is most active) and that there is a distinct interannual variation in their number. The count of extreme events is not well correlated with total seasonal precipitation. The relationship between extreme events and activity in the SACZ is therefore not obvious. From October–
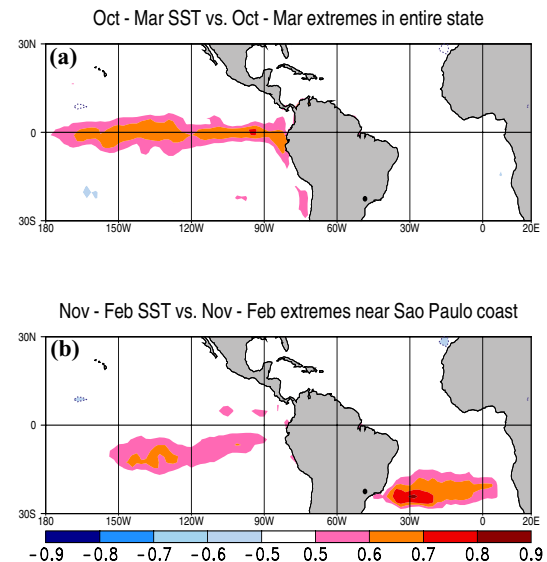

Fig. 4.22. (a) Simultaneous correlation between October–March SST and count of extreme events for during same period in state of São Paulo. An extreme event is counted at each station when daily precipitation exceeds 12% of October–March climatological total. Calculations are for period 1976–1977 to 1994–1995. (b) As in (a) except that correlation is from November–February, stations from which extreme events are counted are in coastal São Paulo, and the 16% level is used as threshold.

March, the interannual count of extreme events in the entire state is correlated positively with sea surface temperature anomalies in the equatorial Pacific from near the dateline to the west coast of South America (**Fig. 4.22a**). The interannual count at stations near the Atlantic coast from November–February is correlated positively with SST anomalies in the Atlantic Ocean near the latitude of São Paulo (**Fig. 4.22b**). In both cases the relationship between SST and mean precipitation is weak. The associations are confirmed with composites and rank correlations.

4.6 Use and evaluation of the NCEP/ NCAR reanalysis

4.6.1 Diurnal modes of variability in reanalysis datasets

The diurnal variability of the diabatic forcing terms and thermodynamic variables in the NCEP and ECMWF reanalysis data sets was investigated. This study aimed to examine the realism of the reanalysis data on very short time scales. Diurnal variability is expected to reveal differences between the two reanalysis data sets because of differences in the physical parameterizations in the two reanalysis models. To narrow the scope of the investigation, we focused on the diurnal (24-hour period) mode of variability in both data sets. **Figure 4.23** shows the amplitude (contours) and phase (arrows, pointing to the maximum; upward = midnight, downward = noon local time) of the diurnal mode of precipitation rate for the NCEP (top) and ECMWF (bottom) reanalyses. The diur-

nal mode of precipitation was found to be significantly different in the two data sets, especially over the central and western Pacific Ocean. The NCEP precipitation has a higher amplitude over the Pacific Ocean. Further analysis of the diurnal cycle (including all harmonics) of precipitation showed that the NCEP precipitation in the western Pacific possesses an early morning maximum (visible in the **top panel of Fig. 4.23**), consistent with in situ observation from TOGA COARE. This characteristic is not well represented in the ECMWF reanalysis data. The diurnal components of all the terms in the column-integrated thermodynamic equation was analyzed for the NCEP reanalysis. Over the ocean, the diurnal tendency of temperature is balanced mainly by the nearly-uniform net (short wave plus long wave) radiative forcing, latent heating (which possesses a similar pattern as precipitation), and adiabatic cooling/heating due to vertical motion. Thus, the diurnal tendency of temperature is substantially influenced by the physical parameterization pertinent to the generation of diurnal precipitation. An important implication of this project is that the error in the short-term variability of a model variable could be rectified into a bias in the long-term climatology. Since the diurnal precipitations in the NCEP and ECMWF reanalyses are significantly different, such a possibility deserves further investigation.
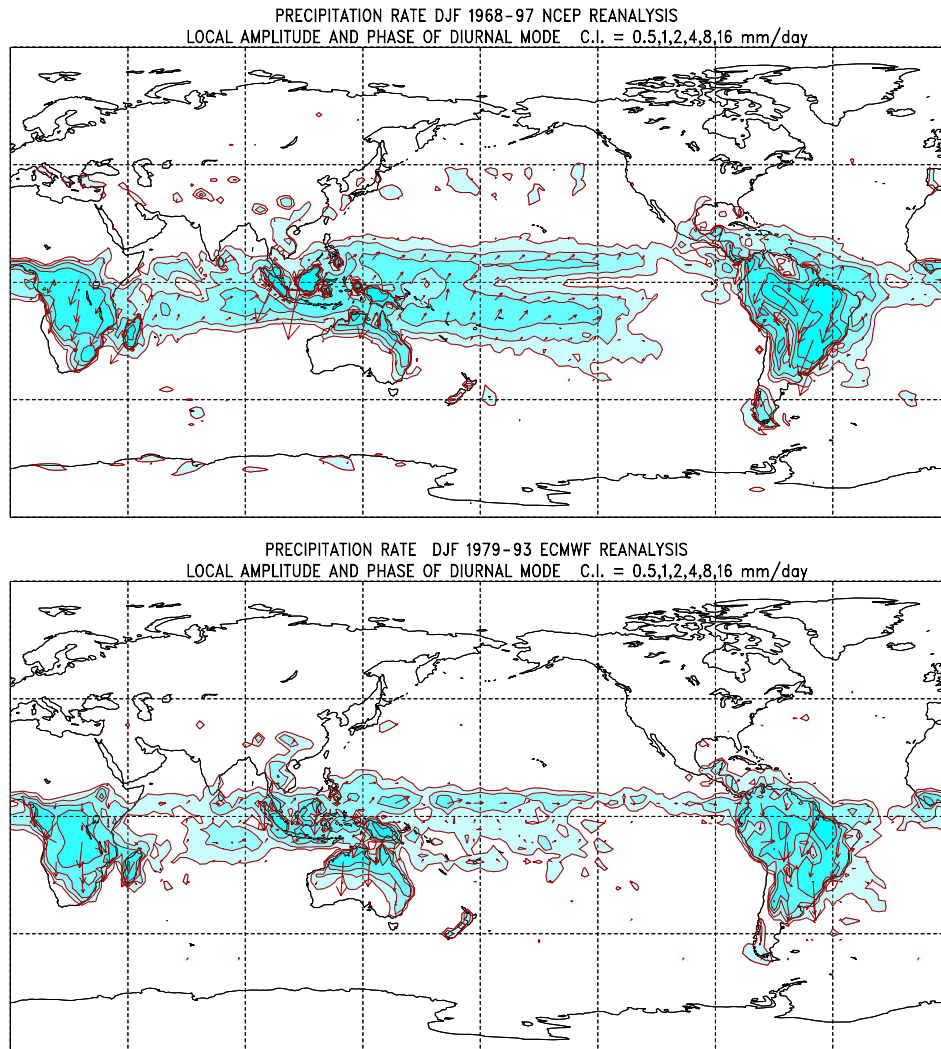
PRECIPITATION RATE DJF 1968-97 NCEP REANALYSIS
LOCAL AMPLITUDE AND PHASE OF DIURNAL MODE   C.I. = 0.5,1,2,4,8,16 mm/day

PRECIPITATION RATE DJF 1979-93 ECMWF REANALYSIS
LOCAL AMPLITUDE AND PHASE OF DIURNAL MODE   C.I. = 0.5,1,2,4,8,16 mm/day

Fig. 4.23. The diurnal (12-hour period) component of precipitation estimated from the NCEP (top) and ECMWF (bottom) reanalyses. The amplitude of precipitation rate is shown in contours, with contour levels 0.5, 1, 2, 4, and 8 mm/day. Areas with amplitude greater than 0.5 mm/day are colored. The phase of the diurnal harmonic is indicated by an arrow pointing to the time of the maximum, upward = 12 AM, downward = 12 PM local time. The analysis is based on winter (Dec.–Feb.) data.

4.6.2 Tropical heating and the chi-problem

To understand the interactions between the tropics and the extratropics, it is important to determine accurately both the climatology and variability of atmospheric heating in the tropics. However, since there are no "heating meters" that may be employed for this purpose, heating is often estimated as a residual in the thermodynamic budget. This means that the vertical profile of horizontal wind divergence must be well specified. To gauge the accuracy of this critical field, we carried out an assessment of the mean

structure and variability of deep convection over the tropical eastern Indian and western Pacific oceans as provided by three different reanalysis datasets for northern winter (DJF) 1980–93. The datasets were generated at the National Centers for Environmental Prediction (NCEP), NASA's Goddard Laboratory for Atmospheres, and the European Center for Medium-range Weather Forecasts (ECMWF). Rainfall, Outgoing Longwave Radiation (OLR), and 200 mb wind divergence fields from the three datasets were compared with one another and with satellite observations.

The internal consistency of the datasets is high, in the sense that the geographical extrema of the rainfall, OLR and divergence fields correspond closely to one another. On the other hand the external consistency, i.e. the agreement between the datasets, is so low as to defy a simple summary. Indeed, the differences are such as to raise fundamental questions concerning: (1) whether there is a single or a split ITCZ over the western Pacific ocean with a strong northern branch, (2) whether there is more convection to the west or the east of Sumatra over the equatorial Indian ocean, and (3) whether there is a relative minimum of convection near New Guinea. Geographical maps of interannual and intraseasonal variances also show similar Order 1 uncertainties, as do regressions against the principal component time series of the Madden-Julian Oscillation (MJO). The annual cycle of convection is also different in each reanalysis. Overall, the ECMWF reanalysis compares best with observa-

tions in this region, but it too has important errors.

Finally, we showed that although the 200 mb divergence fields in the three datasets are highly inconsistent with one another, the 200 mb vorticity fields are highly consistent. This reaffirmed the relevance of diagnosing divergence from knowledge of the vorticity using the method described in Sardeshmukh (1993). This would yield divergence fields from the three datasets that are not only more consistent with each other, but also more consistent with the 200 mb vorticity balance. This iterative procedure was applied to the NCEP/NCAR Reanalysis wind fields (1969–1999) to minimize the vorticity budget residual, and the divergent circulation was further constrained to satisfy the large-scale mass budget. Enforcing dynamical consistency on the divergent circulation had a noticeable effect on the strength, position, and variability of the diagnosed heating extrema. Sub-tropical cooling was also stronger in the chi-corrected dataset. In the tropics, the chi-corrected heating fields showed substantially greater variability, on time scales ranging from daily to seasonal, than the unmodified fields. Vertical profiles of chi-corrected diabatic heating and moistening for the northern winter of 1992–93 compared better with the profiles from observational COARE data than did the profiles from the original reanalyses. Monthly averages of this data have also been made available in atlas form on a CDC web page, http://www.cdc.noaa.gov/chi/.

4.6.3 Tropical surface fluxes

As a by-product of work on the MJO-induced surface fluxes, the reliability of the surface fluxes depicted by the NCEP/NCAR Reanalyses was assessed. On intraseasonal time-scales, fluxes that depend primarily on surface wind variations (e.g., stress and latent heat flux) agree more favorably with direct observations than fluxes that are largely dependent on fluctuations of convection (e.g., surface shortwave radiation and freshwater flux). This is demonstrated for a composite MJO (**Fig 4.24**). While the coherent eastward propagation of stress and latent heat flux are well depicted in the reanalyses, the composite short wave radiation exhibits less than half of the observed amplitude. The direct use of the reanalysis fluxes in studies of the heat budget of the warm pool is thus discouraged. Composite variations of wind stress and latent heat flux from the reanalyses agree better with observations such as during TOGA-COARE.

EPILOGUE

Identifying the role of different physical processes in evolving climate anomalies is a basic component of CDC's research, and is complementary to research to ascertain that physical processes are properly represented in climate models. All five areas of physical process research (Sections 4.1–4.6) will continue to emphasize physical connections and their variations across a broad range of time scales. For example, the linear AAM model does a good job with intraseasonal variations but not with
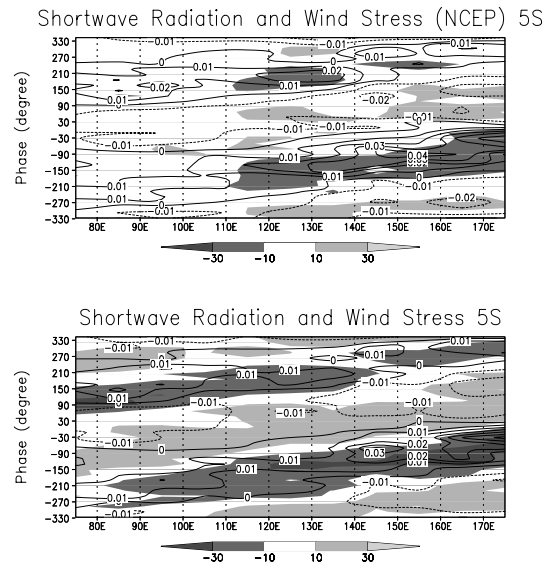

Fig. 4.24. Composite shortwave radiation anomaly (shading) and zonal stress (contours) from NCEP reanalyses (upper panel) and estimates from Shinoda et al. (1998) (lower panel) for the 10 MJO events defined by Shinoda et al. (1998). The vertical axis indicates the phase based on the EOFs of OLR. One cycle is approximately 50 days. The contour interval for stress is 0.01 N m^2 and the shading levels for shortwave radiation are 20 W m^2 with the first shade at +10 and –10 W m^2. Linear trends along the vertical axis are removed.

interannual variability. Stochastic (El Niño) and oscillatory (the QBO) interannual modes can be included in the model and their interactions with intraseasonal variations examined. Indeed, synoptic analyses indicate a link between the transport of momentum across 35N by an interannual mode such as ENSO and excitation of an intraseasonal mid-latitude mode linked with the mountains. Such potential scale interactions of the large scale circulation are of interest both scientifically and for monitoring and prediction purposes.

Air-sea interactions studies related to the MJO will continue with a range of cou-

pled models. One focus will be on proper simulation of the seasonal cycle in the tropics, especially over the Indian Ocean. Model experiments will be designed to test the role of air-sea interaction on the character of monsoonal precipitation fluctuations over South America, including its potential predictability.

Parameterizations of subgrid scale processes in clouds will be implemented in the GFDL Flexible Modeling System, making it more usable for diagnostic studies, and possibly improving its climate. Moist convective parameterizations will be developed and tested to account for the observed variations found across a broad range of time scales and physical environments. Issues of continued interest for parameterization schemes include: the role of cumulus

friction simulated in cloud-resolving models, the non-equilibrium behavior of the diurnal cycle of convection over tropical land masses (**Fig. 4.4**), and the convective organization on relatively small scales (e.g., **Fig. 4.2**) by gravity waves.

Future research in these areas will benefit from new global datasets, from observations made during field projects, and from new climate model datasets. Improving the understanding of basic physical processes will remain essential for diagnosing current climate events, and for evaluating predictions of atmosphere and coupled ocean-atmosphere phenomena.

Contributed by: *J. Bergman, H. Hendon, H.-P. Huang, B. Liebmann, B. Mapes, M. Newman, R. Pincus, P. D. Sardeshmukh, T. Shinoda, and K. Weickmann.*